3D aerogel membrane-based evaporator with sandwich structure for superior solar-driven evaporation

Xi Hu, Yutong Song, Yundi Lv, Beibei Wang, Jinbo Bai, Shenghua Ma

3D aerogel membrane-based evaporator with sandwich structure for superior solar-driven evaporation

Xi Hu [a], Yutong Song [a], Yundi Lv [b], Beibei Wang [a], Jinbo Bai [c,*], Shenghua Ma [a,*]

[a] *State Key Lab Incubation Base of Photoelectric Technology and Functional Materials, International Collaborative Center on Photoelectric Technology and Nano Functional Materials, Institute of Photonics & Photon-Technology, Northwest University, Xi'an 710127, PR China*

[b] *Xi'an Modern Chemistry Research Institute, Xi'an 710065, PR China*

[c] *Université Paris-Saclay, Centrale-Supélec, ENS Paris-Saclay, CNRS, LMPS - Laboratoire de Mécanique Paris-Saclay, 91190, Gif-sur-Yvette, France*

Abstract

Seawater desalination with solar-driven interfacial evaporators has emerged as a promising solution to alleviate global water scarcity. However, conventional two-dimensional (2D) planar evaporators have high reflectivity, which poses a challenge in achieving efficient light absorption. Herein, a sandwich-structured solar-driven interfacial evaporator (SSIE) assembled with three-dimensional (3D) cellulose aerogel membranes (modified with TiN nanoparticles) and an air-laid paper was proposed, which is significantly different from the previously reported 2D membrane-based evaporators. Cellulose aerogel membranes have excellent integrated properties, including extremely high flexibility, allowing for multiple folds, and a 3D porous structure that enables multiple light absorptions. Benefiting from special structural design, SSIE achieves an outstanding evaporation rate of 2.20 kg m^{-2} h^{-1} and an energy efficiency of 83.30%. Moreover, SSIE maintains a stable evaporation rate throughout a 10 h saltwater evaporation process. It also demonstrates excellent performance in seawater and simulated wastewater purification. Furthermore, SSIE exhibits a significant purification effect for dye wastewater, such as Rhodamine B (RhB). This study provides valuable insights into rational structural design for solar evaporators, as well as holding tremendous potential for carrying out seawater desalination in limited spaces.

Keywords: 3D aerogel membrane, Sandwich-structured, TiN nanoparticles, Water supply, Solar-driven interfacial evaporator

1. Introduction

Freshwater resources on the earth are extremely limited, and the threat posed to humanity by water scarcity is exacerbated by the rapid growth of global industry, economy and population [1-4]. It is well-known that the earth has abundant seawater reserves, accounting for approximately 97.5% of the total water resources [5]. Therefore, seawater desalination is an effective technique for producing clean freshwater [6]. Various desalination techniques such as reverse osmosis, multi-effect distillation and multi-stage flash have been developed [7-9]. However, these techniques are relatively complex and costly and can lead to secondary pollution, contradicting the principles of green and sustainable development [10]. Therefore, there is an urgent need to develop clean and green energy approaches to tackle freshwater scarcity [11].

As the most abundant renewable energy resource in nature [12], solar energy has the characteristics of low energy, high efficiency and environmental friendliness, which has been widely utilized in various fields including electricity generation, seawater desalination and sewage treatment [13]. Thus, utilizing solar steam generation technology to produce clean freshwater holds promising prospects [14-16]. This technology uses photothermal materials to absorb sunlight and convert it into heat, enhancing vapor production [17]. The vapor subsequently gradually condenses and is collected to produce freshwater [14]. Traditional methods involve thermally energizing the entire volume of water by dispersing the photothermal materials in water [18]. However, the traditional approach leads to substantial loss of heat to the bulk water, giving rise to a lower efficiency of water evaporation and hindering its large-scale practical applications [19]. In recent years, researchers have proposed an efficient and low-cost approach for desalination by applying photothermal evaporators with localized interfacial heating, which involves an interface between air and water, to solar steam generation [20, 21]. These floating photothermal evaporators concentrate the absorbed solar energy for conversion and steam generation at the water-air interface [22]. In this way, only the interfacial water is locally heated, while the volume of water remains closer to the ambient temperature, thus increasing the conversion efficiency of photothermal energy and minimizing heat loss [23]. Solar-driven interfacial evaporators typically consist of photothermal materials and porous substrates [24]. An ideal solar interfacial evaporator needs to meet three criteria simultaneously: (i) high light absorption within the solar wavelength range to

maximize the conversion of solar energy to heat; (ii) efficient thermal management to minimize heat loss; and (iii) rational water transport to ensure continuous water supply to the evaporative surface [25, 26].

To enhance the photothermal conversion efficiency, various types of materials have been explored for solar-driven interfacial evaporation, including metallic materials [14, 27], carbon-based materials [13, 28], semiconductors [29], plasmonic nanomaterials [30], and polymer materials [8, 25], among others. Transition metal nitrides have demonstrated significant potential in solar-driven interfacial evaporation techniques due to their strong ability to absorb solar energy [31]. Titanium nitride (TiN), as a transition metal nitride, exhibits strong surface plasmonics photothermal effects similar to metallic nanoparticles, efficiently converting light into heat [32]. This makes TiN a promising candidate material for developing photothermal structures. Various structural designs of solar-driven interfacial evaporators based on TiN have been developed, such as 2D thin film materials [32], 3D aerogels and hydrogels [2, 33]. However, 2D planar structures often suffer from high light reflection and thermal radiation losses, resulting in decreased evaporation rates [34]. 3D structures benefit from increased evaporation surface area, allowing more energy to be collected from the surrounding environment and bulk water, leading to higher evaporation rates and energy efficiency [28]. As a result, the study of 3D evaporators is gaining popularity [35]. Cellulose aerogels are known for their porous structure, which facilitates multiple reflections of light within the pores and minimizes energy losses [36]. In addition, cellulose aerogels offer a large specific surface area, stable mechanical properties and rich hydroxyl groups on the surface, making them easily modifiable [37]. Therefore, cellulose aerogels are an excellent choice for the construction of 3D solar evaporators.

Rational water transport is another crucial factor in the construction of solar evaporators [38]. Cellulose aerogels, due to excellent hydrophilicity, are typically in direct contact with bulk water to ensure a timely water supply. However, the rapid water supply results in a significant amount of unevaporated water within the aerogel, leading to overall heating similar to traditional solar evaporation. This wastes the absorbed energy from the photothermal material, increases the thermal conductivity of the aerogel, weakens the localized heating effect and reduces the evaporation rate [39]. On the other hand, inadequate water supply causes local drying and salt accumulation, reducing the effective evaporation area [40]. Researchers have made efforts to achieve

reasonable water transport. For instance, Zou et al. [40] designed an arched structure with grooves and microcavities on the surface, allowing for the formation of a 3D continuous water film and a confined liquid layer underneath, thus maintaining the continuity of the water film and ensuring sufficient liquid replenishment. Zhang et al. [41] used the method of free-water evaporation to manufacture adjustable water transport channels, which regulate the water supply capability of the material. Nonetheless, efficient design strategies that involve accurate control of moisture content within the material and specialized surface structures exposed at the heating interface face significant challenges such as complicated manipulation, high cost and bad material stability [39]. Therefore, the development of efficient design strategies still presents considerable obstacles in terms of moisture content control and the creation of stable surface structures exposed to heated interfaces.

Here, we presented a novel self-floating sandwich-structured evaporator using freeze-drying. A hydrophobic cellulose/TiN aerogel membrane (HCTAM) was used as the top layer for photothermal conversion. An air-laid paper (AP) was employed as an intermediate water transport layer with two channels for water transfer. The bottom layer consisted of a hydrophobic pure cellulose aerogel membrane (HCAM) serving as an insulating layer. The evaporator proposed by this work is made of cellulose aerogel membranes, which not only retain the advantages of traditional membrane materials such as portability and flexibility, but also address the limitation of high light reflection in 2D structures, enabling efficient sunlight absorption and minimizing energy loss. Benefiting from remarkable insulation, efficient water transport channels, and reliable light absorption capacity, SSIE achieves a high evaporation rate of about 2.20 kg m^{-2} h^{-1} and an impressive energy efficiency of around 83.30% under 1 sun irradiation. Furthermore, it demonstrates a stable performance in seawater desalination within a 10 h cycle, maintaining a stable evaporation rate. The material cost of SSIE is approximately \$6.37 m^{-2}, which is lower than most of the evaporators that have been reported. In conclusion, the developed sandwich-structured evaporator holds significant potential for clean water production and provides insights into the efficient structural design of solar evaporators.

2. Experimental

2.1. Materials

Quantitative filter paper was purchased from Hangzhou Special Paper Industry Co., Ltd. Air-laid paper was purchased from Taobao. Urea (≥99.0%) was supplied by Sinopharm Chemical Reagent Co., Ltd. Sodium hydroxide (NaOH, ≥96.0%) was obtained from Tianli Chemical Reagent Co., Ltd. Titanium nitride (TiN NPs; average particle size~20 nm; >99.9%) and Methyltrichlorosilane (MTCS, 99.0%) were bought from Macklin Biochemical Technology Co., Ltd. Rhodamine B (RhB) and N'N-Methylenebisacrylamide (MBA, ≥99,0%) were bought from Comeo Reagents Co., Ltd. Deionized water is prepared in the laboratory. These chemicals required no pretreatment before use.

2.2 Preparation of HCTAM

HCTAM-30% was prepared using a simple solution casting and vacuum freeze-drying method. Firstly, 0.61 g of shredded filter paper was dissolved in 13.5 ml of pre-cooled alkaline solution (NaOH: urea: DI = 7:12:81). The mixture was stirred by magnetic stirring for 2 h in an ice bath. Subsequently, 0.183 g of TiN nanoparticles (constituting 30% of the cellulose mass) were added to a cellulose solution and stirred for 1 h to form a black cellulose/TiN solution. The mixture was then sonicated for 15 minutes to achieve a uniform dispersion. The cellulose/TiN solution was stored in a refrigerator for later use. Next, 0.183 g of MBA (crosslinking agent) was added to the cellulose/TiN solution and magnetically stirred for 1 h. The resulting mixture was poured into a culture dish, and the bubbles were removed in a vacuum drying chamber for 15 min. It was left to age for 24 h to form a hydrogel membrane. The hydrogel membrane was repeatedly rinsed with deionized water until pH reached neutrality. Finally, the hydrogel membrane was vacuum freeze-dried for 72 h to obtain a hydrophilic cellulose/TiN aerogel membrane.

Hydrophobic modification of cellulose/TiN aerogel membranes was performed using chemical vapor deposition. In detail, 1 ml of MTCS was placed in a sealed container together with an aerogel membrane. The sealed container was then placed in a vacuum drying oven at 55℃ for 12 h. After the reaction was completed, hydrophobic cellulose/TiN aerogel membrane was obtained. The same method was used to prepare a hydrophobic pure cellulose aerogel membrane.

The cellulose/TiN aerogel membranes were prepared using the same method, with TiN nanoparticles occupying 10% and 50% of the cellulose mass, respectively. They were named HCTAM-10% and HCTAM-50%. The thicknesses of HCTAM-30% and HCAM used in this study were 1 mm, and the details are discussed in the

supporting information.

2.3. Preparation of SSIE

The SSIE was prepared using a facile physical assembly method. In detail, the air-laid paper was cut to the same size as the prepared aerogel membrane, while retaining two water supply channels of width 1cm. Then, the air-laid paper was placed between two layers of aerogel membranes (the upper layer being HCTAM-30% and the lower layer being HCAM), with the two water supply channels placed in water to transfer water to the heating interface.

2.4. Characterizations

The morphology and elemental composition of the aerogel membrane and air-laid paper were obtained employing a field emission scanning electron microscope (SEM, FEI Apreo S). The crystal structures of aerogel membranes were investigated using an X-ray diffractometer (XRD, Bruker D8 ADVANCE). Fourier-transform infrared spectroscopy (FTIR, Bruker Optics Tensor 27) was employed to record the spectra in the range of 500-4000 nm. XPS spectra were observed utilizing X-ray photoelectron spectroscopy (XPS, PHI5000 Versa Probe III). A contact angle analyzer (DSA25) was utilized to measure the water contact angles of aerogel membranes. The transmission and reflectance spectra of the samples were taken using a UV-vis-NIR spectrophotometer (UV-vis-NIR，PerkinElmer Lambda 950). The thermal conductivities of the aerogel membrane were measured within the temperature range of 20-100°C using a laser flash analyzer (LFA 467, NETZSCH). An inductively coupled plasma emission spectrometer (ICP, Optima 2100DV) was used to detect the concentration of metal ions in seawater, wastewater, and collected water samples.

2.5. Solar steam generation performance test

The experiment was conducted by a solar light simulator (PL-X300DF) with a filter. The energy intensity of sunlight was examined by a photometer (CEL-NP 2000 Full spectrum Strong light power meter). During the illumination process, the mass change of water was recorded using an electronic balance (BSA224S, Sartorius, accuracy 0.1 mg). The infrared camera (FLIR-T5590) was utilized to take infrared images and surface temperatures of the samples. The ambient temperature and humidity were maintained at 25 ± 2 ℃ and $45 \pm 5\%$, respectively. The water evaporation efficiency was obtained using the following equations:

$$\eta_{evp} = \left(\nu_e E_{equ}\right)/Q_{solar} \quad (1)$$

Where ν_e (kg m^{-2} h^{-1}) represents the evaporation rate, E_{equ} (kJ kg^{-1}) is the actual evaporation enthalpy (the detailed method is provided in the Supporting Information), and Q_{solar} (kJ m^{-2} h^{-1}) is the energy intensity irradiated on the evaporator.

3. Results and discussion

3.1. Structure design of SSIE

A sandwich-structured solar-driven interfacial evaporator based on cellulose aerogel membranes was fabricated using freeze-drying and layer-by-layer assembly techniques, as illustrated in Fig. 1 (see Experimental section for details). SSIE consists of three parts. The topmost layer is composed of HCTAM-30%. TiN nanoparticles are superior light-absorbing materials with stable properties. The vertical vessels in the cellulose aerogel membrane act as perfect light traps. The sunlight can be reflected many times before being finally absorbed by the HCTAM-30%. Therefore, HCTAM-30% acts as a light-absorbing layer. The middle layer is formed by AP, which retains two water supply channels for continuous water transfer. The bottom layer utilizes HCAM as a thermal insulating layer to prevent heat loss to the bulk water. Moreover, HCAM provides mechanical support to ensure the entire evaporator floats on the surface of the water.

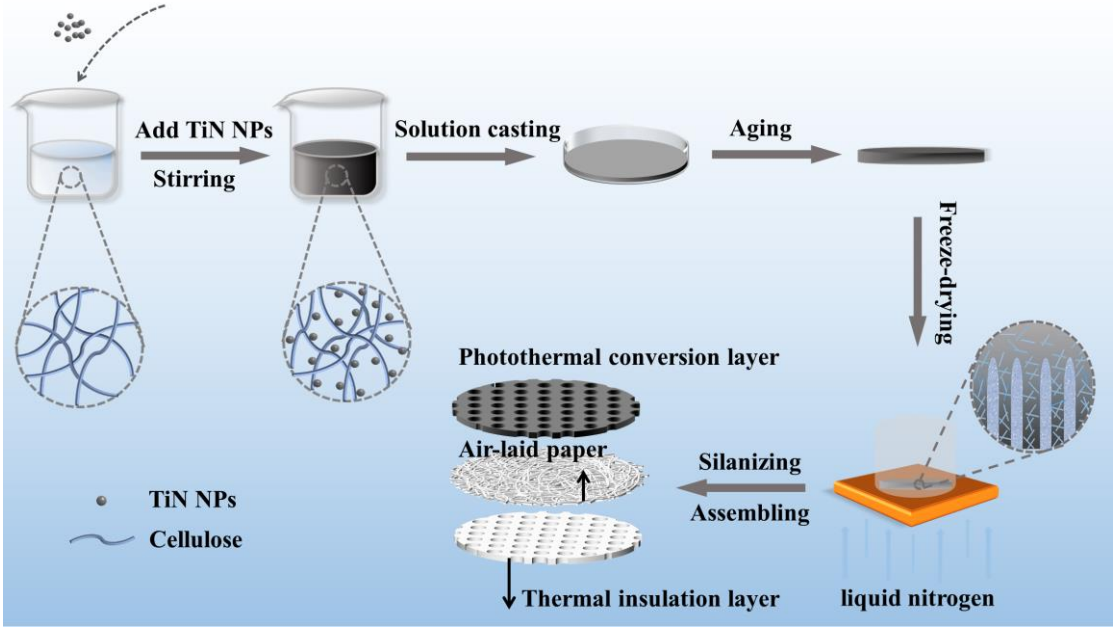

Fig. 1. The preparation process of SSIE.

3.2. Morphology and characterization of SSIE

The morphology and internal structure of the SSIE are shown in Fig. 2. Figs. 2a and 2d represent the morphological characteristics of HCAM, which exhibits an open interconnected porous structure and pore diameter is between 200 and 300 μm approximately. The side view reveals vertically arranged vessels that effectively organize air convection, minimize thermal radiation and conduction and possess excellent heat-insulating properties. Fig. 2b displays the surface morphology of AP, which is porous and features disordered arranged fibers. HCTAM-30% appears black and has vertically aligned micro-pores that serve as optical traps to enhance the photothermal effect of TiN nanoparticles (Figs. 2c and 2e). Moreover, the micro-pores facilitate the release of steam. The elemental composition of the HCAM and HCTAM-30% surfaces are depicted in Figs. S1a and S1b, respectively. Furthermore, The TEM image is shown in Fig. 2f, the grain sizes of TiN nanoparticles attached to the cellulose surface range from 20 to 30 nm. The elemental mapping clearly shows the distribution of C, O, Si, Ti, and N elements in HCTAM-30%, which confirmed the successful combination of TiN nanoparticles and cellulose. According to Fig. 2g, the cellulose aerogel membrane demonstrates outstanding flexibility, allowing for multiple folds without compromising its integrity. Even after being bent and folded numerous times, the membrane quickly regained its original shape with only a few creases on the surface, thus highlighting its exceptional flexibility.

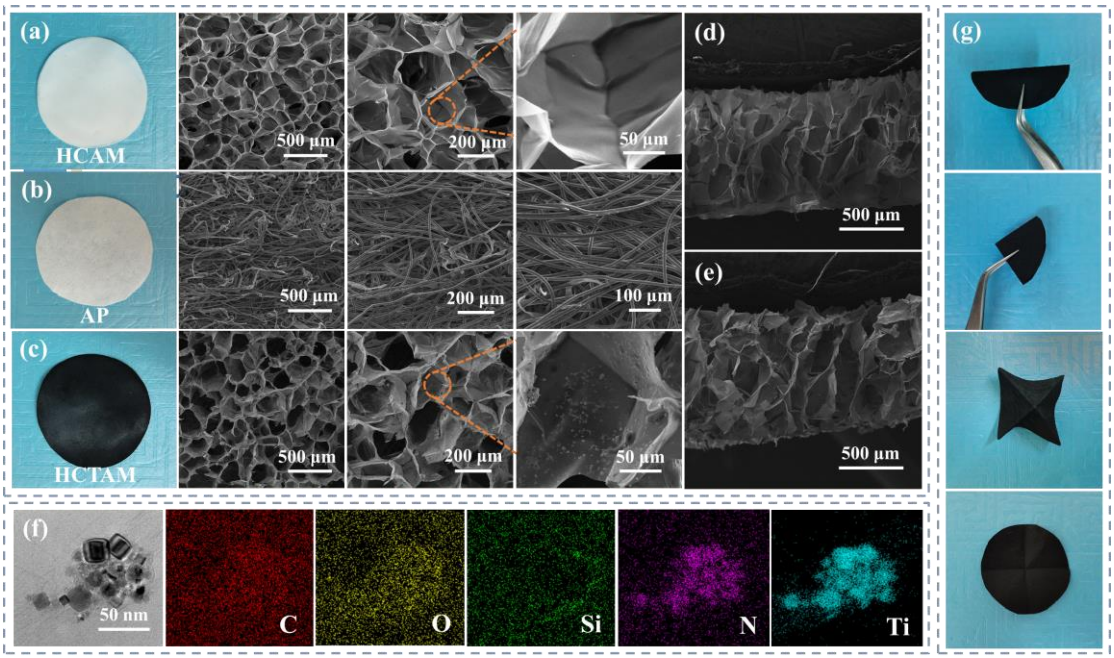

Fig. 2. (a-c) HCAM, AP and HCTAM-30% images and SEM images. (d) HCAM cross-section morphology. (e) HCTAM-30% cross-section morphology. (f) TEM image of TiN NPs in cellulose surface and elemental mapping images. (g) The images of HCTAM-30% undergoing bending and folding.

The crystalline structures of CAM and CTAM are illustrated in Fig. 3a. Cellulose displays sharp diffraction peaks at 15.2°, 17.1°, 22.9°, and 34.7°, corresponding to the (101), (10-1), (200) and (004) crystal planes. Apart from these characteristic cellulose diffraction peaks, CTAM exhibited distinct diffraction peaks of TiN at 36.8°, 42.8°, 62.0°, 74.3°, and 78.2°, representing the (111), (200), (220), (311) and (222) crystal planes, indicating successful integration of cellulose and TiN.

The surface element composition and chemical state of CTAM were further investigated. Fig. 3b displays the full spectrum of CAM and CTAM, revealing the presence of N peaks (399.0 eV). These peaks suggest the successful combination of TiN and cellulose. For the C 1s spectrum of CTAM (Fig. 3c), it is located at the peaks of ≈284.3 eV, ≈286.1 eV, and ≈287.6 eV, corresponding to the C-C, C-O, and C=O bonds, respectively. The two sub-peaks of O 1s (Fig. 3d) are ≈531.1 eV (C=O) and ≈532.2 eV (C-O). In the Ti 2p spectrum (Fig. 3e), the deconvolution peaks ≈463.1 eV and ≈456.7 eV, ≈458.8 eV and ≈455.1 eV, and ≈457.8 eV and ≈453.7 eV correspond to the Ti-O_x, intermediate TiO_xN_y and Ti-N in TiN nanoparticles, respectively [1].

Furthermore, hydrophobic modifications on CAM and CTAM were performed. As shown in Fig. 3f, the chemical structural characteristics of the samples were investigated by Fourier transform infrared spectroscopy (FTIR). Both HCAM and

HCTAM-30% exhibit stretching vibrations of O-H at around 3342 cm^{-1}. Additionally, the stretching vibrations at 1058 cm^{-1} and 1645 cm^{-1} corresponded to C=O, C=C, and C-O-C bonds. Moreover, vibrations of Si-CH_3 and Si-O-Si were observed at 1272 cm^{-1} and 780 cm^{-1}, indicating the formation of a silicon-oxygen network. This observation was further confirmed by the surface elemental composition (Fig. S1) and water contact angle measurements (Fig. 4a, b).

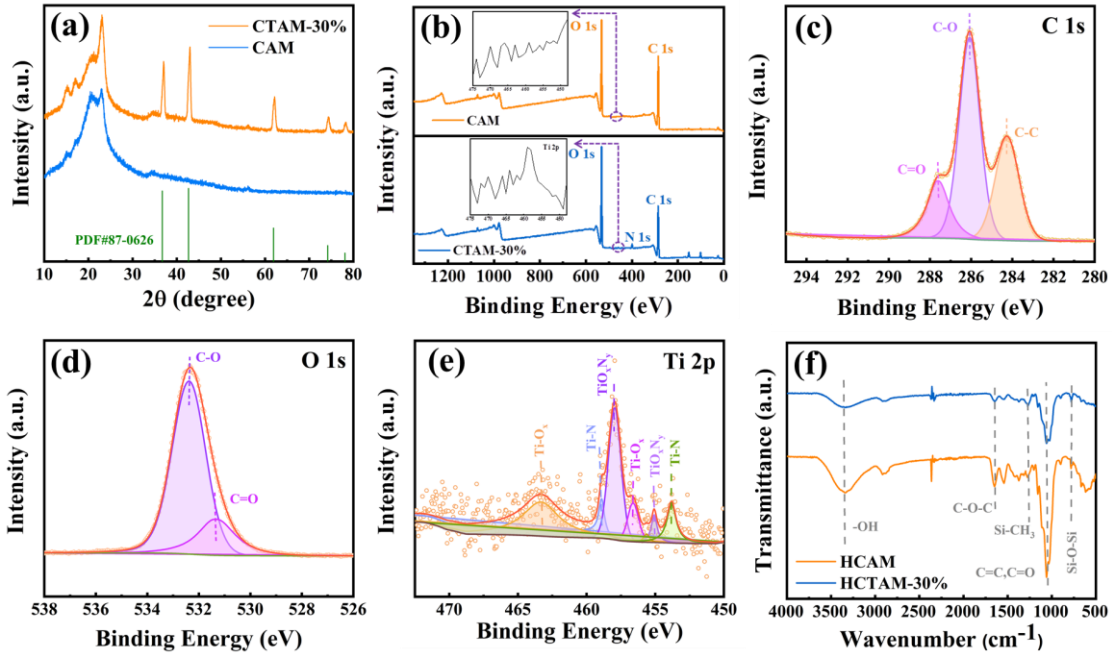

Fig. 3. (a) XRD images of CAM and CTAM. (b) XPS full spectrum of CAM and CTAM. (c) C 1s spectrum of CTAM. (d) O 1s spectrum of CTAM. (e) Ti 2p spectrum of CTAM. (f) FTIR spectra of HCAM and HCTAM-30%.

3.3. Water transfer mechanism of SSIE

Rational water transport plays a crucial role in achieving efficient solar water evaporation. Excessive water supply leads to excessive heat loss and reduces the evaporation rate, whereas insufficient water supply leads to localized dryness or salt accumulation, thereby diminishing the effective evaporation area. In this study, a sandwich-structured evaporator based on the different wetting properties was constructed. The HCTAM-30% layer served as the solar absorber, and the AP acted as the water transport layer (Fig. 4a, b, c demonstrate the water contact angle). Here we delve into water evaporation by analyzing the water transport process. During the transmission process, water is primarily influenced by two forces: hydrostatic pressure (P_H) and Laplace pressure (P_L):

$$P_H = \rho g h \tag{5}$$

$$P_L = \frac{2\gamma}{R_l} \tag{6}$$

Where ρ is the density of water, g represents the acceleration of gravity, h is the height of the droplet, γ is the surface tension of water, and R_l is the curvature radius of the solid-liquid interface. In Fig. 4d, for the HCTAM-30% layer, water molecules are hindered from passing through due to the P_L acting in the opposite direction to the hydrostatic pressure. For fully hydrophilic air-laid paper, water molecules can spontaneously migrate upward along the water supply route through capillary forces and diffuse along the surface of the air-laid paper (as shown in Fig. 4e and Fig. S4). However, for the fully air-laid paper, excessive water supply may occur, leading to unnecessary heat loss. Due to the close contact between the hydrophilic and hydrophobic layers, when water molecules reach the surface of the air-laid paper and come into contact with the hydrophobic layer, two competing forces are generated: P_L and P_H (Fig. 4f). The total pressure of water in the evaporator can be calculated as follows:

$$\Delta P = P_H - P_L = \rho g h - \frac{2\gamma}{R_l} \tag{7}$$

When $P_H > P_L$, water molecules can flow through and fill the hydrophobic layer. Upon contact with the hydrophobic layer, the Laplace pressure P_L controls the movement of water molecules and suppresses rapid water transport, providing an adequate water supply.

Simultaneously, as sunlight penetrates the evaporator surface, the temperature of the surface rises, intensifying the kinetic energy of water molecules and diminishing interfacial tension. The relationship between temperature and interfacial tension is as follows:

$$\gamma V_m^{2/3} = k(T_C - T - 6.0) \tag{8}$$

Where k is a constant, V_m represents the volume of water, and T_C denotes the critical temperature. From the equation, it can be observed that as T approaches the critical

temperature, the surface tension tends to zero. Consequently, when water is transported to the top layer, water vapor escapes more easily. Simultaneously, the decrease in interfacial tension leads to a lower Laplace pressure, allowing water molecules to be transported to the evaporation surface, thereby achieving a balance between water supply and evaporation. As depicted in Figure S5, the highest evaporation rate was obtained for SSIE compared to the hydrophilic photothermal layer and a single hydrophobic photothermal layer, confirming that SSIE achieves a balance between water supply and evaporation. Therefore, this structure with varying wetting properties presents an advantage for implementing solar-driven seawater desalination.

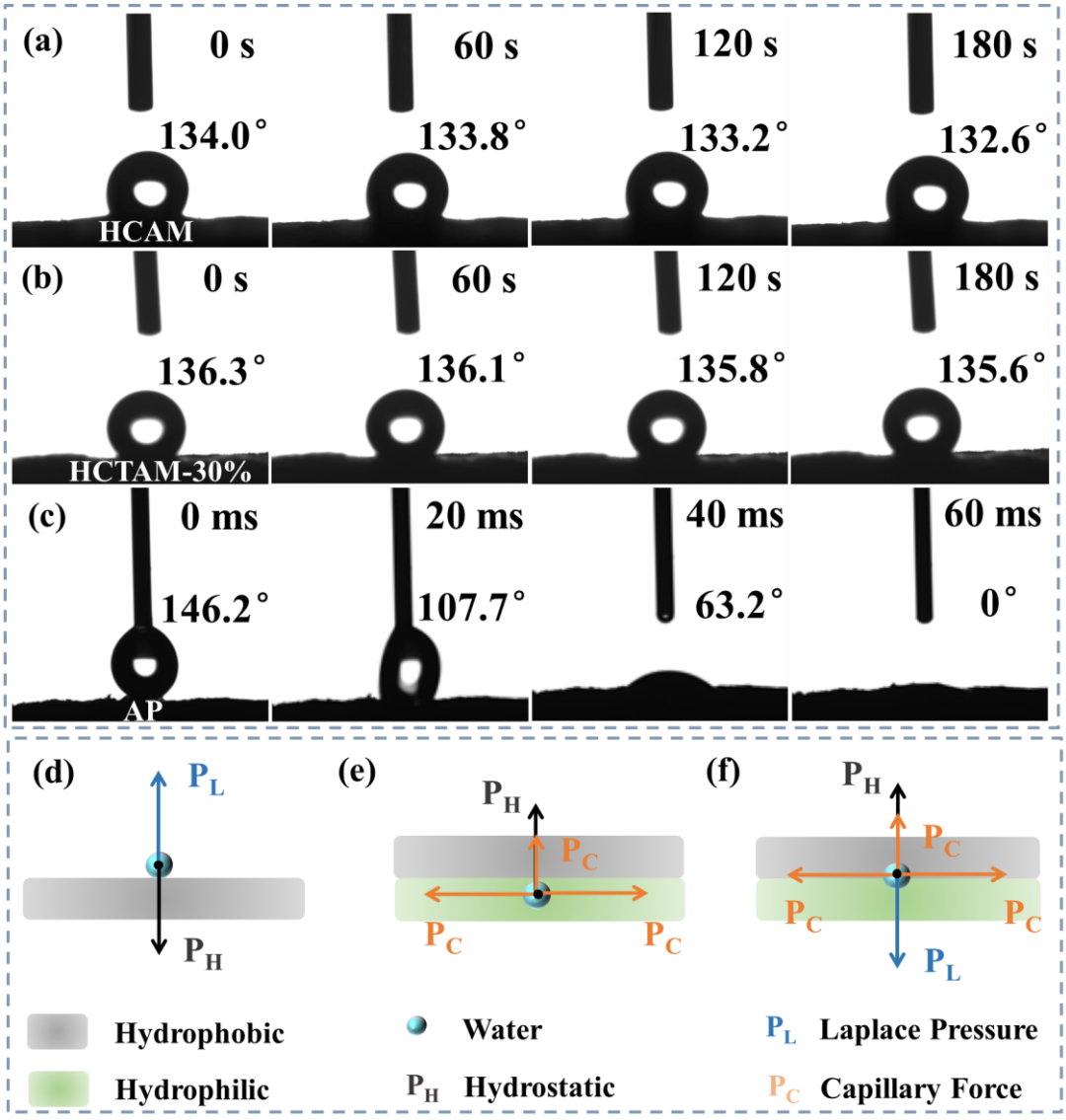

Fig. 4. Water contact angle of (a) HCAM, (b) HCTAM-30% and (c) AP. Mechanism of water transport: (d) The water droplet on the HCTAM-30% was blocked arising from the Laplace pressure; (e) The penetration behavior of water droplets from the hydrophilic AP side to the

HCTAM-30% side; (f) When water droplets reach the interface between hydrophilic and hydrophobic, the Laplace pressure is created.

3.4. Light absorption and photothermal conversion of SSIE

The efficient absorption of solar radiation is another crucial factor in achieving a high solar evaporation rate. To evaluate this, various key indicators of SSIE were measured, including solar absorption and surface temperature changes. As shown in Fig. 5a, the HCTAM-30% has a stronger light-absorbing capability compared to the HCAM sample across a wider range of solar wavelengths (300-2500nm), resulting in approximately 99% full-spectrum absorption (absorbance A = 1-R-T). Additionally, HCTAM-30% also demonstrates lower transmittance (T) and reflectance (R) (Fig. S7a-b). The excellent light-absorbing capability of HCTAM-30% can be attributed not only to the inherent broadband absorption of TiN nanoparticles (Fig. 5a) but also to its higher porosity (Fig. S8). Fig. 5b displays the comparative photothermal conversion capabilities of HCTAM-30%, HCAM and pure water under 1 sun. The time-temperature curve demonstrates that HCTAM-30% possesses superior photothermal conversion capacity. Within just 3 min, the surface temperature rapidly increases from 25.0℃ to 43.8℃, and within 20 min, it reaches equilibrium, stabilizing at 49.8± 0.3℃. This temperature is approximately 15.3℃ higher than that of pure water, confirming the exceptional light-heat conversion capability of HCTAM-30%. Infrared images confirm the temperature variation on the sample surface (Fig. 5c). Additionally, for efficient solar energy utilization in practical applications, it is crucial to maintain rapid water transport while minimizing heat loss. Therefore, the HCAM was utilized as a thermal insulation layer to mitigate heat dissipation into the bulk water. The thermal insulating capacity of HCAM is illustrated in Fig. 5d, which exhibits a relatively low thermal conductivity coefficient of approximately 0.032 $Wm^{-1}k^{-1}$. Furthermore, Fig. S9 demonstrates the temperature variability of the bulk water under 1 sun, highlighting the crucial role of the low thermal conductivity of HCAM in minimizing heat dissipation into the bulk water and confining the heat within the evaporation zone. The evaporation system diagram is shown in Fig. 5e. All these results demonstrate that SSIE exhibits excellent photothermal conversion capability and outstanding thermal management capacity, enabling efficient implementation of solar-driven seawater desalination.

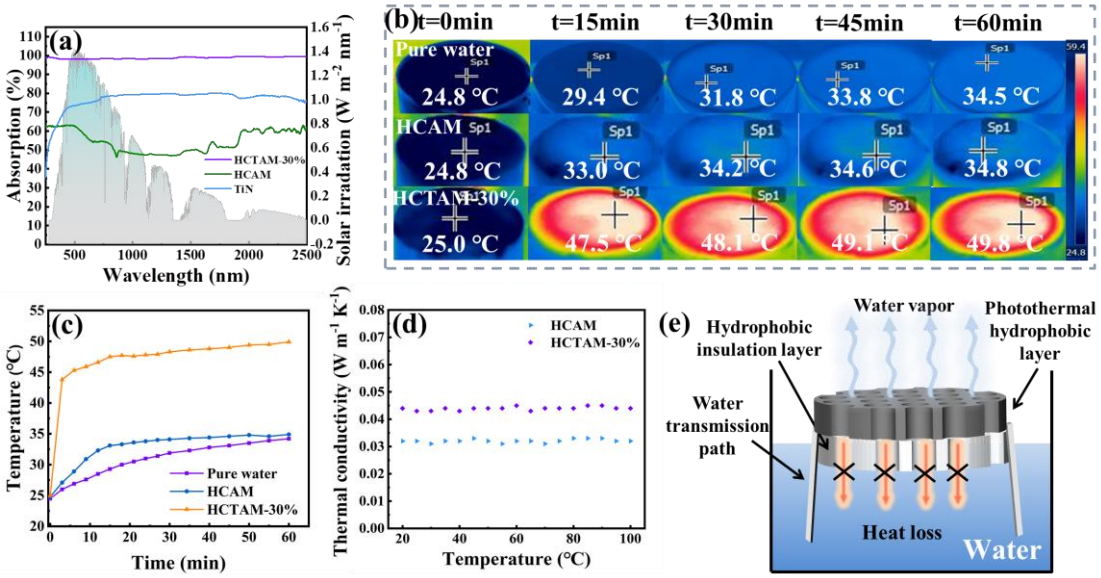

Fig. 5. (a) Absorption spectrum of SSIE in the wet state. (b) The surface temperature changes of pure water, HCAM and HCTAM-30% under irradiation of 1 kW m^{-2}. (c) The infrared thermal images of pure water, HCAM and HCTAM-30% under irradiation of 1 kW m^{-2}. (d) The thermal conductivity of HCAM and HCTAM-30% at different temperatures. (e) The evaporation system diagram of SSIE.

3.5. Solar-driven water evaporation performance of SSIE

Due to the superior photothermal properties of HCTAM, the water evaporation performance of SSIE was investigated using the testing system depicted in Fig. S10. The experiment was performed at a room temperature of approximately 25°C, with air humidity ranging from 40% to 50%. To measure the change of water mass due to vapor escape, an electronic balance was employed, while an infrared thermal imaging camera recorded the surface temperature of the SSIE. Fig. 6a illustrates the mass change of different TiN concentrations in the HCTAM layer (10%, 30% and 50% by mass of cellulose) under 1 sun. Notably, it can be observed that when TiN accounts for 30% of the cellulose mass, the highest mass change per unit time was recorded, reaching a peak evaporation rate of 2.20 Kg m^{-2} h^{-1}, which is approximately 6 times the evaporation rate of pure water (0.36 Kg m^{-2} h^{-1}). SSIE exhibited a higher evaporation rate than the thermodynamic evaporation limit (~1.46 kg m^{-2} h^{-1}), probably attributed to the low evaporation enthalpy. The evaporation enthalpy of pure water was ≈2410 KJ kg^{-1}. It can be observed from Table S2 that the evaporation enthalpy of HCTAM-30% decreased to 1363.09 KJ Kg^{-1}. This is because the

hydrophobicity of the photothermal layer reduces the evaporation work of water, thereby lowering the evaporation enthalpy of water. On the other hand, the hydrophilic functional groups on the hydrophilic layer weaken the hydrogen bonds between water molecules, also contributing to the reduction of the evaporation enthalpy. The energy efficiency of the SSIE was calculated using Equation (1) to evaluate its energy utilization efficiency. The corresponding trend between energy conversion efficiency and the evaporation rate is shown in Fig. 6b. The energy conversion efficiencies of pure water, HCAM, HCTAM-10%, HCTAM-30% and HCTAM-50% are 22.77%, 59.32%, 81.80%, 83.30% and 71.69%, respectively, under 1 sun illumination. This result highlights the advantages of SSIE in terms of energy utilization, due to the outstanding thermal management capability of SSIE and its efficient water transport. Moreover, the SSIE demonstrates long-lasting durability and stability during a 10 h cyclic test, as depicted in Fig. 6c. Further investigations were carried out on various properties of the SSIE under different illumination conditions. To further investigate the evaporation performance of SSIE under different weather conditions, the evaporation rates were measured under 0.3 sun to 7 sun. As shown in Figs. 6d and 6e, the evaporation rate of SSIE increased from 0.89 Kg m^{-2} h^{-1} to 7.83 Kg m^{-2} h^{-1} under seven different solar radiation intensities. The surface temperature achieved a maximum of 94°C, which increased by approximately 45°C compared to 1 sun illumination alone (Fig. 6f). These results indicate that SSIE has a strong environmental adaptability.

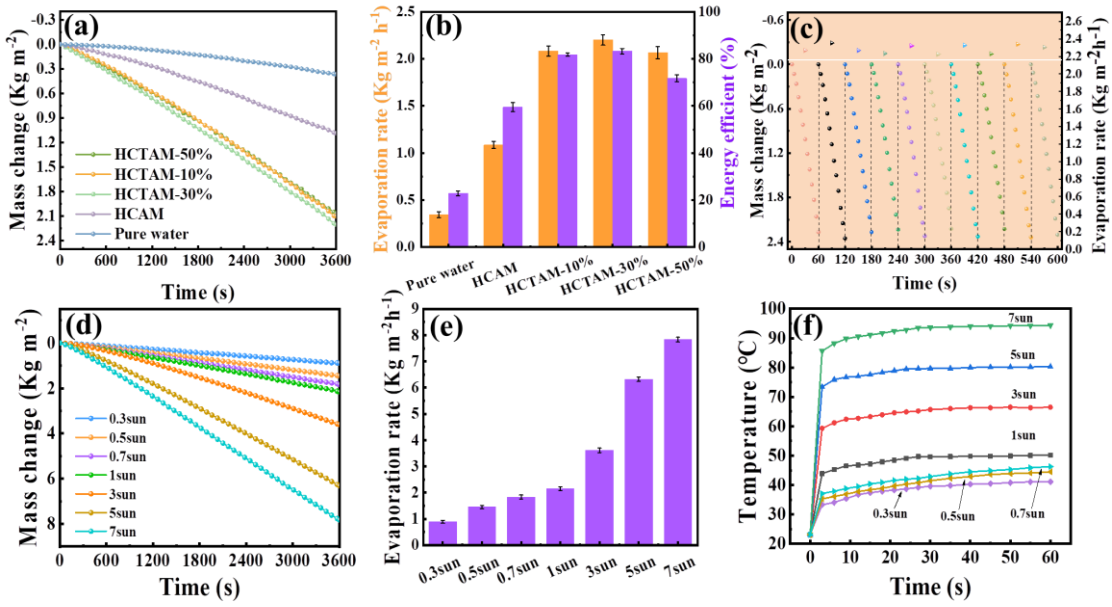

Fig. 6. (a) Mass change of SSIE with different proportions of TiN under 1sun. (b) Evaporation rate and energy efficiency of SSIE with different proportions of TiN under 1sun. (c) Mass change and

evaporation rate of the SSIE were tested in pure water for 10 h. (d) Mass change of SSIE under 0.3, 0.5, 0.7, 1,3,5,7 sun. (e) Evaporation rate of SSIE under 0.3, 0.5, 0.7, 1,3,5,7 sun. (f) The surface temperature changes of SSIE in 1,3,5,7 sun.

For the purpose of evaluating the evaporation performance in saltwater, the SSIE was tested in solutions containing 2%, 3.5%, 7% and 10% NaCl. The evaporation rates in the 3.5% and 10% sodium chloride solutions could reach 2.01 Kg $m^{-2} h^{-1}$ and 1.78 Kg $m^{-2} h^{-1}$, respectively (Fig. 7a,b). Fig. 7c presents the results of a continuous 10-hour test, showing that the steam generation rate of SSIE remains nearly constant in both pure water and 3.5% NaCl solution. In addition, the inset shows that there is no salt accumulation on the SSIE surface throughout the 10-hour test (the detailed salt-resistance mechanism is discussed in the supporting information). This indicates the potential of using SSIE in highly saline seawater. It is worth noting that the SSIE is more competitive than similar materials already reported (Fig. 7d) [42-61]. Compared to single-type membrane-based evaporators and aerogel-based evaporators, the cellulose aerogel membrane retains the original characteristics of bulk aerogel (lightweight, porous, heat insulation).

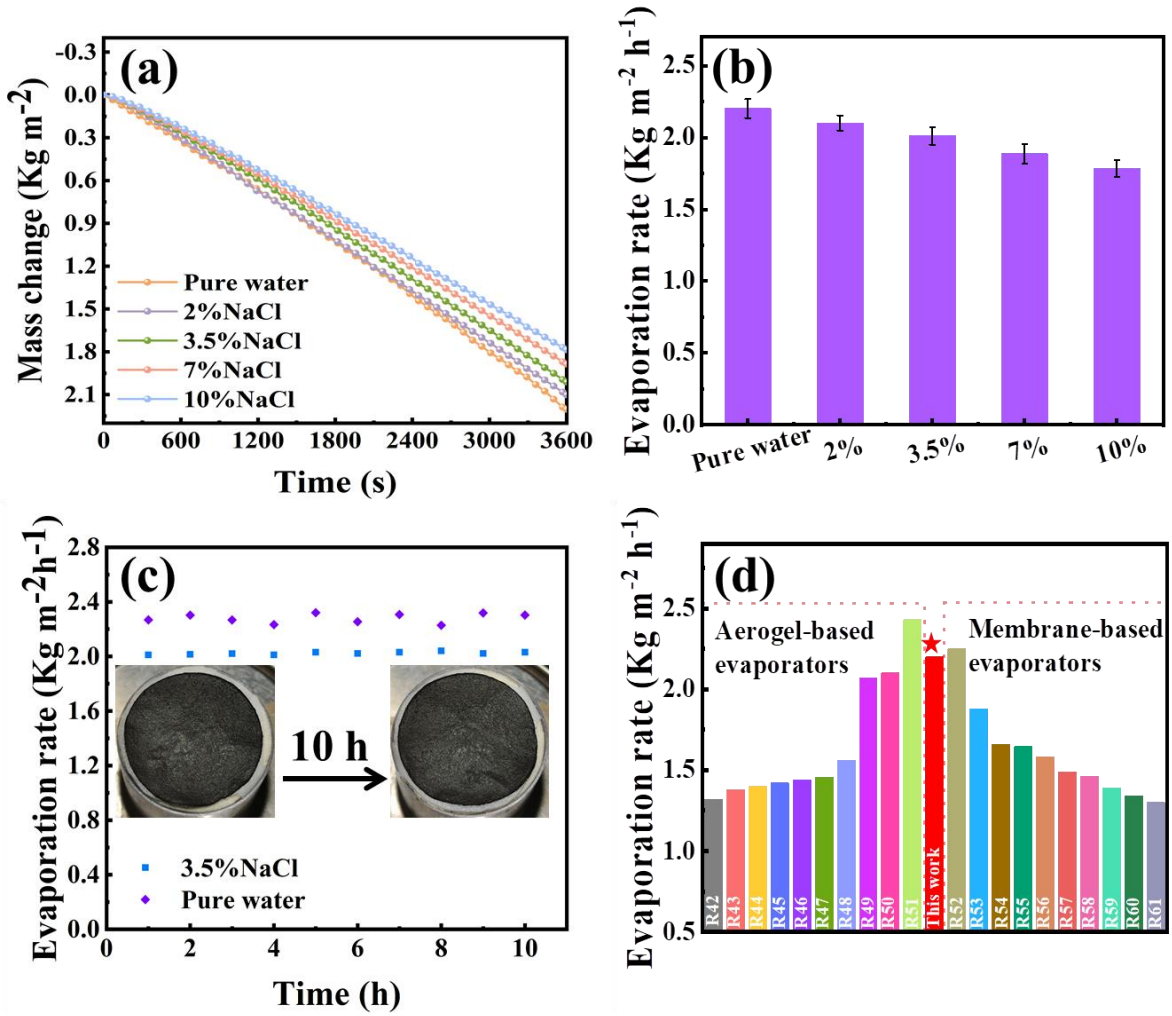

Fig. 7. (a) Mass change of SSIE using pure water and NaCl solutions with various salinities. (b) Evaporation rates of SSIE in pure water and NaCl solutions with various salinities. (c) Evaporation rates of the SSIE was tested in pure water and 3.5% NaCl solutions for 10 h. (d) Comparison of the evaporation rate of the evaporator prepared in this work with that of the evaporators reported.

3.6. Seawater purification performance of SSIE

To evaluate the practicality of SSIE, a water vapor collection device was used (Fig. S12) to capture the water vapor generated by sunlight. The seawater used in the experiment was sourced from the Bohai Sea. The contents of four main ions (Na^+, Mg^{2+}, K^+, Ca^{2+}) in the water samples were determined using an Inductively Coupled Plasma Emission Spectrometer, as shown in Fig. 8a. Following the desalination process, the ion concentration experienced a significant decrease by three to four magnitudes, falling well below the drinking water quality standards established by the

WHO and the EPA. Also, the purification experiment was conducted on artificially simulated wastewater containing heavy metal ions, the results of which are shown in Fig. 8b. After purification, the contents of heavy metal ions were lower than the WHO standard for drinking water. Additionally, a water evaporation experiment was performed using simulated polluted water containing RhB (9 mg/L) as the contaminant. The strong absorption peak of RhB (553nm) in the collected condensate almost disappeared (Fig. 8c). Furthermore, we tested the water quality of the purified seawater and wastewater using an ohmmeter, with the resistances reflecting the water quality (Fig. 8d). The resistances measured for seawater, simulated wastewater, purified seawater and purified wastewater were 0.508 MΩ, 0.331 MΩ, 4.02 MΩ and 4.70 MΩ, respectively, demonstrating the effectiveness of seawater desalination.

The working performance of SSIE in strong acid and strong alkaline solutions was further evaluated. Fig. 8e presents the evaporation performance of SSIE in 1mol/L NaOH and 1mol/L H_2SO_4 solutions. The evaporation rates in 1mol/L NaOH and 1mol/L H_2SO_4 solutions are 1.94 Kg m^{-2} h^{-1} and 1.95 Kg m^{-2} h^{-1}, respectively. The pH values of the collected condensate water are close to neutral (Fig. 8f). These results indicate that SSIE exhibits excellent evaporation performance in strong acid and strong alkali solutions.

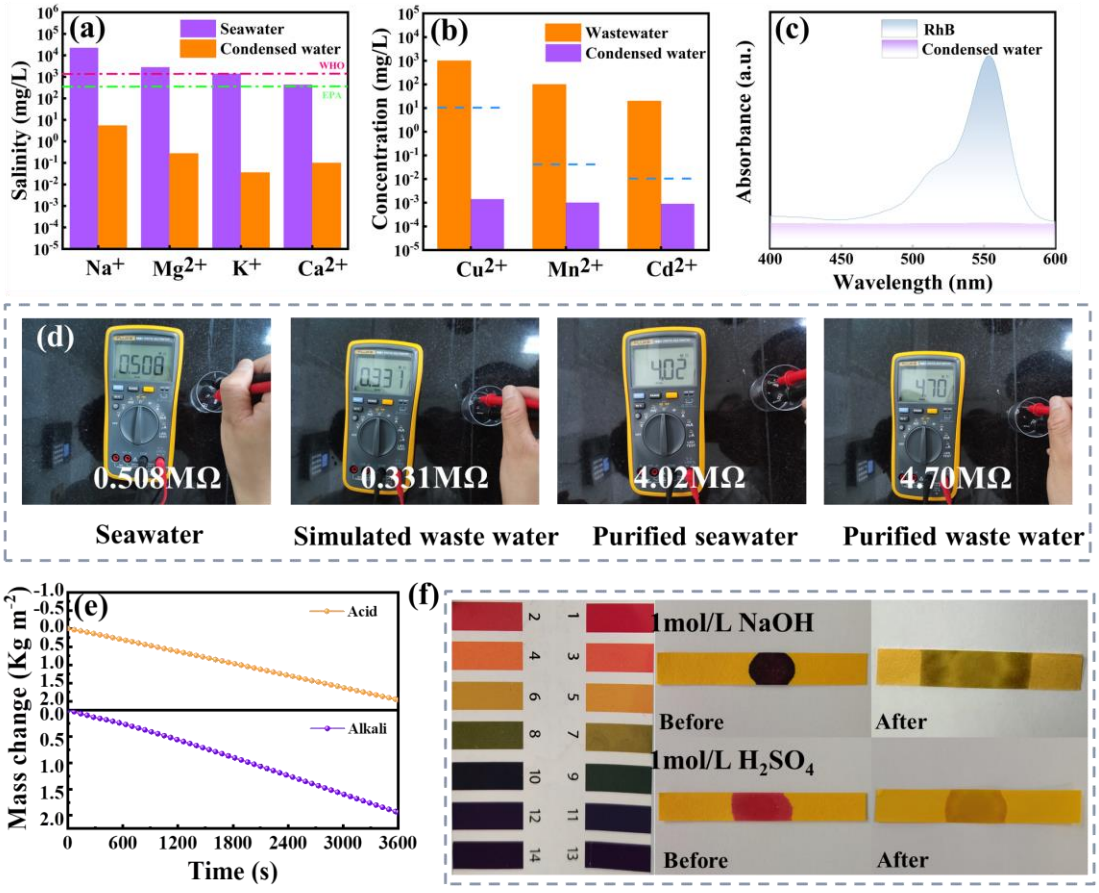

Fig. 8. Ions concentrations in purified seawater (a) and purified wastewater (b). (c) UV absorption spectra of RhB as wastewater solutions before and after purification. (d) Measurement of resistance between electrodes to evaluate water purity. (e) Mass change of SSIE in strong acids and alkali. (f) pH values of the strong acid and alkali solution, and the purified water.

3.7. Outdoor evaporation experiment of SSIE

To assess the practical application of SSIE, an outdoor evaporation experiment was conducted on the campus of Northwest University in Xi'an (2023, 10, 14). The whole evaporation experiment was conducted from 8:30 a.m. to 6:30 p.m., and lasted for 10 h. During the evaporation experiment, the outdoor temperature, solar radiation intensity, and ambient humidity were obtained through the Northwest University Geographical and Ecological Observation Network. Fig. 9a shows the schematic diagram of the outdoor evaporation setup. The transparent glass cover is used to collect condensed water quickly. As the internal temperature is higher than the external temperature, water vapor condenses on the inner surface of the glass cover and is collected. The variations of ambient temperature, relative humidity and solar radiation intensity are shown in Fig. 9b. The real environment is different from a

controlled laboratory setting, and in outdoor experiments, solar radiation intensity and environmental conditions have a significant impact on water evaporation performance. Fig. 9c depicts the outdoor evaporation rate of SSIE, which can reach a maximum evaporation rate of 1.42 Kg m^{-2} h^{-1}. It indicates that SSIE exhibits excellent evaporation performance and strong environmental adaptability.

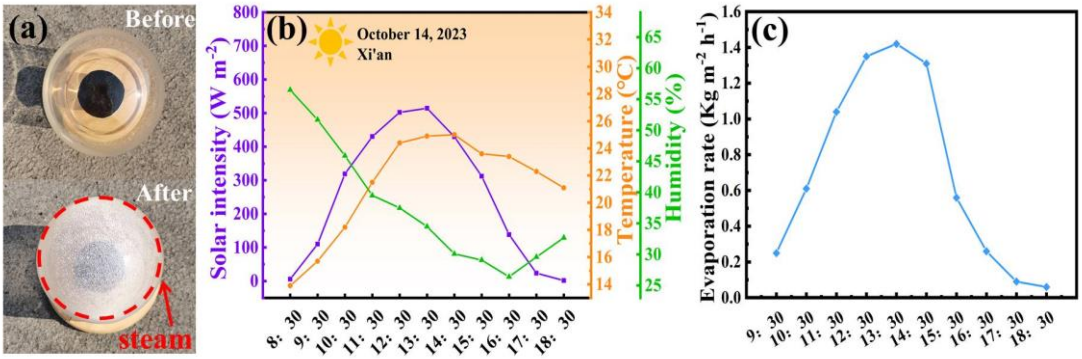

Fig. 9. (a) The outdoor evaporation setup of SSIE. (b) Solar radiation intensity, ambient temperature and relative humidity at different times during the experiment. (c) The evaporation rates of SSIE at different time intervals.

4. Conclusion

In conclusion, a sandwich-structured solar interfacial evaporator made of cellulose aerogel membrane was prepared, which successfully achieved an impressive evaporation efficiency of up to 83.30% and an exceptional solar steam generation rate of 2.20 Kg m^{-2} h^{-1}. The unique sandwich structure and water supply route enable efficient water transport and minimize heat loss, contributing to the improved performance of the solar interfacial evaporator. Additionally, the SSIE maintains a stable evaporation rate during a 10 h process using a 3.5% NaCl solution. Excellent results have also been obtained in seawater and wastewater purification. Therefore, this study provides a rational strategy for designing solar evaporators and demonstrates great potential in practical applications for desalinating seawater.

CRediT authorship contribution statement

Xi Hu: Investigation, Methodology, Data curation, Writing – original draft. **Yutong Song:** Investigation, Methodology. **Yundi Lv:** Investigation. **Beibei Wang:** Investigation. **Jinbo Bai:** Supervision, Project administration. **Shenghua Ma:**

Supervision, Methodology, Writing – review & editing, Funding acquisition.

Declaration of competing interest

The authors declare that they have no known competing financial interests or personal relationships that could have appeared to influence the work reported in this paper.

Acknowledgments

This work was supported by the National Natural Science Foundation of China (No. 52002320), the Science Foundation of Shaanxi Province (No.2022GD-TSLD-18), the China Postdoctoral Science Foundation (No.2022M712574).

5. References

[1] Y. Wang, X. Liu, Q. Zhang, C. Wang, S. Huang, Y. Liu, T. Yu, R. Yang, G. Chen, M. Chaker and D. Ma, Stable, Cost‐Effective TiN‐Based Plasmonic Nanocomposites with over 99% Solar Steam Generation Efficiency, Adv. Funct. Mater. 333 (2023) 2212301, https://doi.org/10.1002/adfm.202212301.

[2] Y. Tian, X. Liu, S. Xu, J. Li, A. Caratenuto, Y. Mu, Z. Wang, F. Chen, R. Yang, J. Liu, M. L. Minus and Y. Zheng, Recyclable and efficient ocean biomass-derived hydrogel photothermal evaporator for thermally-localized solar desalination, Desalination 523 (2022) 115449, https://doi.org/10.1016/j.desal.2021.115449.

[3] X. Zheng, Y. Bao, A. Huang, G. Qin and M. He, 3D printing double-layer hydrogel evaporator with surface structures for efficient solar steam generation, Sep. Purif. Technol. 306 (2023) 122741, https://doi.org/10.1016/j.seppur.2022.122741.

[4] S. Cheng, Z. Sun, Y. Wu, P. Gao, J. He, Z. Yin, L. Liu and G. Li, A thermally insulated solar evaporator coupled with a passive condenser for freshwater collection, J. Mater. Chem. A 9 (2021) 22428-22439, https://doi.org/10.1039/d1ta05781b.

[5] L. Chen, X. Mu, Y. Guo, H. Lu, Y. Yang, C. Xiao and Q. Hasi, MXene-doped kapok fiber aerogels with oleophobicity for efficient interfacial solar steam generation, J. Colloid Interface Sci. 626 (2022) 35-46, https://doi.org/10.1016/j.jcis.2022.06.143.

[6] Y.-Q. Luo, F. Song, X.-L. Wang and Y.-Z. Wang, Water bridge solar evaporator with salt-resistance and heat localization for efficient desalination, J. Mater. Chem. A 11 (2023) 3118-3125, https://doi.org/10.1039/d2ta09244a.

[7] J. Zhu, J. Liu, J. Liu, S. Guo, S. Lu, Y. Lv and B. Song, FDM 3D-printed volcanic-shaped structure for ultrafast solar-driven interfacial evaporation and efficient energy utilization, Desalination 548 (2023) 116275, https://doi.org/ 10.101 6 /j.desal.2022.116275.

[8] H. W. Lim, S. H. Park and S. J. Lee, 3D thermoresponsive hydrogel with enhanced water uptake and active evaporation for effective interfacial solar steam generation, Desalination 550 (2023) 116368, https://doi.org/10.1016/j.desal.202 2.116368.

[9] X. Gu, C. Fan and Y. Sun, Multilevel design strategies of high-performance interfacial solar vapor generation: A state of the art review, Chem. Eng. J. 460 (2023) 141716, https://doi.org/10.1016/j.cej.2023.141716.

[10] H. Yao, P. Zhang, C. Yang, Q. Liao, X. Hao, Y. Huang, M. Zhang, X. Wang, T. Lin, H. Cheng, J. Yuan and L. Qu, Janus-interface engineering boosting solar steam towards high-efficiency water collection, Energy Environ. Sci. 14 (2021) 5330-5338, https://doi.org/10.1039/d1ee01381e.

[11] Z. Fan, J. Ren, H. Bai, P. He, L. Hao, N. Liu, B. Chen, R. Niu and J. Gong, Shape-controlled fabrication of MnO/C hybrid nanoparticle from waste polyester for solar evaporation and thermoelectricity generation, Chem. Eng. J. 451 (2023) 138534, https://doi.org/10.1016/j.cej.2022.138534.

[12] Y. Zhu, G. Tian, Y. Liu, H. Li, P. Zhang, L. Zhan, R. Gao and C. Huang, Low-Cost, Unsinkable, and Highly Efficient Solar Evaporators Based on Coating MWCNTs on Nonwovens with Unidirectional Water-Transfer, Adv. Sci. 8 (2021) e2101727, https://doi.org/10.1002/advs.202101727.

[13] K. Yu, P. Shao, P. Meng, T. Chen, J. Lei, X. Yu, R. He, F. Yang, W. Zhu and T. Duan, Superhydrophilic and highly elastic monolithic sponge for efficient solar-driven radioactive wastewater treatment under one sun, J. Hazard. Mater. 392 (2020) 122350, https://doi.org/122350,10.1016/j.jhazmat.2020.122350.

[14] L. Noureen, Z. Xie, Y. Gao, M. Li, M. Hussain, K. Wang, L. Zhang and J. Zhu, Multifunctional Ag(3)PO(4)-rGO-Coated Textiles for Clean Water Production by Solar-Driven Evaporation, Photocatalysis, and Disinfection, ACS Appl. Mater Interfaces 12 (2020) 6343-6350, https://doi.org/10.1021/acsami.9b16043.

[15] Y. Geng, K. Zhang, K. Yang, P. Ying, L. Hu, J. Ding, J. Xue, W. Sun, K. Sun and M. Li, Constructing hierarchical carbon framework and quantifying water transfer for novel solar evaporation configuration, Carbon 155 (2019) 25-33, https://doi.org/10.1016/j.carbon.2019.08.055.

[16] Q. Ma, P. Yin, M. Zhao, Z. Luo, Y. Huang, Q. He, Y. Yu, Z. Liu, Z. Hu, B. Chen and H. Zhang, MOF-Based Hierarchical Structures for Solar-Thermal Clean Water Production, Adv. Mater. 31 (2019) e1808249, https://doi.org/10.1002/adma.201808249.

[17] Z. Wei, Y. Wang, C. Cai, Y. Zhang, S. Guo, Y. Fu and S. C. Tan, Dual‐Network Liquid Metal Hydrogel with Integrated Solar‐Driven Evaporation, Multi‐Sensory Applications, and Electricity Generation via Enhanced Light Absorption and Bénard–Marangoni Effect, Adv. Funct. Mater. 32 (2022) 2206287, https://doi.org/10.1002/adfm.202206287.

[18] C. Du, X. Zhao, X. Qian, C. Huang and R. Yang, Heat-localized solar evaporation: Transport processes and applications, Nano Energy 107 (2023) 108086 https://doi.org/10.1016/j.nanoen.2022.108086.

[19] H. Gao, N. Bing, Z. Bao, H. Xie and W. Yu, Sandwich-structured MXene/wood aerogel with waste heat utilization for continuous desalination, Chem. Eng. J. 454 (2023) 140362, https://doi.org/10.1016/j.cej.2022.140362.

[20] W. Zhang, T. Zheng, H. Zhu, D. Wu, C. Zhang and H. Zhu, Insight into the role of the channel in photothermal materials for solar interfacial water evaporation, Renewable Energy 193 (2022) 706-714, https://doi.org/10.1016/j.renene.2022.04.139.

[21] J. Wang, Z. Zhao, C. Yang, M. Sun, J. Chen, Y. Zhou and H. Xu, Marine biomass metal-organic framework hybrid evaporators for efficient solar water purification, Desalination 556 (2023) 140383, https://doi.org/10.1016/j.desal.2023.116577.

[22] L. Chen, J. Ren, J. Gong, J. Qu and R. Niu, Cost-effective, scalable fabrication of self-floating xerogel foam for simultaneous photothermal water evaporation and thermoelectric power generation, Chem. Eng. J. 454 (2023) 140383, https://doi.org/10.1016/j.cej.2022.140383.

[23] A. Wang, H. Liang, F. Chen, X. Tian, S. Yin, S. Jing and P. Tsiakaras, Facile synthesis of C3N4/NiIn2S4 heterostructure with novel solar steam evaporation efficiency and photocatalytic H2O2 production performance, Appl. Catal. B 310 (2022) 121336, https://doi.org/10.1016/j.apcatb.2022.121336.

[24] M. K. Alam, M. He, W. Chen, L. Wang, X. Li and X. Qin, Stable and Salt-Resistant Janus Evaporator Based on Cellulose Composite Aerogels from Waste Cotton Fabric, ACS Appl. Mater. Interfaces 14 (2022) 41114-41121, https://doi.org/10.1021/acsami.2c12750.

[25] S. Wang, Y. Fan, F. Wang, Y. Su, X. Zhou, Z. Zhu, H. Sun, W. Liang and A. Li, Potentially scalable fabrication of salt-rejection evaporator based on electrogenerated polypyrrole-coated nickel foam for efficient solar steam generation, Desalination 505 (2021) 114982, https://doi.org/10.10 16/j.desal.2021.114982.

[26] C. Liu, C. Cai and X. Zhao, Overcoming Salt Crystallization During Solar Desalination Based on Diatomite-Regulated Water Supply, ACS Sustain. Chem.Eng. 8 (2020) 1548-1554, https://doi.org/10.1021/acssuschemeng.9b06102.

[27] Z. Guo, F. Yu, Z. Chen, Z. Shi, J. Wang and X. Wang, Stabilized Mo2S3 by FeS2 based porous solar evaporation systems for highly efficient clean freshwater collection, Sol. Energy Mater Sol. Cells 211 (2020) 110531, https://doi.org/10.1016/j.solmat.2020.110531.

[28] Y. Wang, X. Wu, T. Gao, Y. Lu, X. Yang, G. Y. Chen, G. Owens and H. Xu, Same materials, bigger output: A reversibly transformable 2D–3D photothermal evaporator for highly efficient solar steam generation, Nano Energy 79 (2021) 105477, https://doi.org/10.1016/j.nanoen.2020.105477.

[29] G. Zhu, J. Xu, W. Zhao and F. Huang, Constructing Black Titania with Unique Nanocage Structure for Solar Desalination, ACS Appl. Mater. Interfaces 8 (2016) 31716-31721, https://doi.org/10.1021/acsami.6b11466.

[30] Y. Zhang, Y. Wang, B. Yu, K. Yin and Z. Zhang, Hierarchically Structured Black Gold Film with Ultrahigh Porosity for Solar Steam Generation, Adv. Mater. 34 (2022) e2200108, https://doi.org/10.1002/adma.202200108.

[31] H. Yu, D. Wang, H. Jin, P. Wu, X. Wu, D. Chu, Y. Lu, X. Yang and H. Xu, 2D MoN1.2 ‐ rGO Stacked Heterostructures Enabled Water State Modification for Highly Efficient Interfacial Solar Evaporation, Adv. Funct. Mater. 33 (2023) 2214828, https://doi.org/10.1002/adfm.202214828.

[32] M. U. Farid, J. A. Kharraz, P. Wang and A. K. An, High-efficiency solar-driven water desalination using a thermally isolated plasmonic membrane, J. Clean.Prod. 271 (2020) 122684, https://doi.org/10.1016/j.jclepro.2020.122684.

[33] Z. Gui and D. Xiang, Hierarchically designed evaporators with dual-layered

hydrogel/aerogel structure for efficient solar water evaporation, Sep. Purif. Technol. 310 (2023) 123237, https://doi.org/10.1016/j.seppur.2023.123237.

[34] Z. Lei, X. Sun, S. Zhu, K. Dong, X. Liu, L. Wang, X. Zhang, L. Qu and X. Zhang, Nature Inspired MXene-Decorated 3D Honeycomb-Fabric Architectures Toward Efficient Water Desalination and Salt Harvesting, Nanomicro Lett 14 (2021) 10, https://doi.org/10,10.1007/s40820-021-00748-7.

[35] Y. Bu, Y. Zhou, W. Lei, L. Ren, J. Xiao, H. Yang, W. Xu and J. Li, A bioinspired 3D solar evaporator with balanced water supply and evaporation for highly efficient photothermal steam generation, J. Mater. Chem. A 10 (2022) 2856-2866, https://doi.org/10.1039/d1ta09288j.

[36] X. Han, S. Ding, L. Fan, Y. Zhou and S. Wang, Janus biocomposite aerogels constituted of cellulose nanofibrils and MXenes for application as single-module solar-driven interfacial evaporators, J. Mater. Chem. A 9 (2021) 18614-18622, https://doi.org/10.1039/d1ta04991g.

[37] A. S. Norfarhana, R. A. Ilyas and N. Ngadi, A review of nanocellulose adsorptive membrane as multifunctional wastewater treatment, Carbohydr. Polym. 291 (2022) 119563, https://doi.org/10.1016/j.carbpol.2022.119563.

[38] X. Zhang, X. Wang, W. D. Wu, X. D. Chen and Z. Wu, Self-floating monodisperse microparticles with a nano-engineered surface composition and structure for highly efficient solar-driven water evaporation, J. Mater. Chem. A 7 (2019) 6963-6971, https://doi.org/10.1039/c8ta12290c.

[39] X. Zhang, D. Xiang, K. Deng, Y. Zhan, X. Liu and B. Shang, Sandwich-structured evaporator with multilayer confined heating interface for boosting solar vapor generation, Chem. Eng. J. 450 (2022) 137988, https://doi.org/10.1016/j.cej.2022.137988.

[40] M. Zou, Y. Zhang, Z. Cai, C. Li, Z. Sun, C. Yu, Z. Dong, L. Wu and Y. Song, 3D Printing a Biomimetic Bridge-Arch Solar Evaporator for Eliminating Salt Accumulation with Desalination and Agricultural Applications, Adv. Mater. 33 (2021) e2102443, https://doi.org/10.1002/adma.202102443.

[41] X. Zhang, T. Li, W. Liao, D. Chen, Z. Deng, X. Liu and B. Shang, A water supply tunable bilayer evaporator for high-quality solar vapor generation, Nanoscale 14 (2022) 7913-7918, https://doi.org/10.1039/d2nr01595a.

[42] Q. Guo, H. Yi, F. Jia and S. Song, Vertical porous MoS2/hectorite double-layered aerogel as superior salt resistant and highly efficient solar steam generators,

Renewable Energy 194 (2022) 68-79, https://doi.org/10.1016/j.renene.2022.05.051.

[43] Z. Chen, Y. Luo, Q. Li and X. Chen, Microgroove-Structured PDA/PEI/PPy@PI-MS Photothermal Aerogel with a Multilevel Water Transport Network for Highly Salt-Rejecting Solar-Driven Interfacial Evaporation, ACS Appl. Mater. Interfaces 13 (2021) 40531-40542, https://doi.org/10.1021/acsami.1c09155.

[44] D. You, W. Yang, Y. Zhao, H. Yu, Y. Ma, D. Lin, Q. Pan and S. Song, Salt-tolerant and low-cost flame-treated aerogel for continuously efficient solar steam generation, Solar Energy 227 (2021) 303-311, https://doi.org/10.1016/j.solener.2021.09.024.

[45] T. Xue, F. Yang, X. Zhao, F. He, Z. Wang, Q. Wali, W. Fan and T. Liu, Portable solar interfacial evaporator based on polyimide nanofiber aerogel for efficient desalination, Chem. Eng. J. 461 (2023) 141909, https://doi.org/10.1016/j.cej.2023.141909.

[46] M. Zhang, F. Xu, W. Liu, Y. Hou, L. Su, X. Zhang, R. Zhang, L. Zhou, X. Yan, M. Wang, X. Hou and Y. Cao, Antibacterial evaporator based on reduced graphene oxide/polypyrrole aerogel for solar-driven desalination, Nano Res. 16 (2022) 4219-4224, https://doi.org/10.1007/s12274-021-4041-4.

[47] W. Mu, Y. Yu, H. Sun, Z. Zhu, J. Li and W. Liang, Fabrication of ATP/PEG/MnO(2)NWs composite for solar steam generation with high conversion efficiency, J. Colloid Interface Sci. 648 (2023) 916-924, https://doi.org/10.1016/j.jcis.2023.06.063.

[48] J.-K. Xiao, J.-Z. Gong, M. Dai, Y.-F. Zhang, S.-G. Wang, Z.-D. Lin, F.-P. Du and P. Fu, Reduced graphene oxide/Ag nanoparticle aerogel for efficient solar water evaporation, J. Alloys Comp. 930 (2023) 167404, https://doi.org/10.1016/j.jallcom.2022.167404.

[49] H. Duan, M. Wang, Z. Zhang, J. Zhen and W. Lv, Biomass-derived photothermal carbon aerogel for efficient solar-driven seawater desalination, J. Environ. Chem. Eng. 11 (2023) 109295, https://doi.org/10.1016/j.jece.2023.109295.

[50] Y. Yuan, X. Han, H. Cai, K. Yang, S. Zhang, X. Li and M. Zhang, Co-Assembled WS2 Nanosheets/Chitosan Aerogels with Oriented Micro-Channels for Efficient and Sustainable Solar Steam Generation, ACS Sustain. Chem. Eng. 11 (2023) 4643-4651, https://doi.org/10.1021/acssuschemeng.2c06472.

[51] Y. Ren, G. Zhang, H. Hui, Z. Guo, M. Tian and Q. Zhang, Design of a

Pyrrole/Polyimide fiber-based Janus aerogel to suppress salt deposition and enhance solar steam generation performance, Desalination 562 (2023) 116712, https://doi.org/10.1016/j.desal.2023.116712.

[52] S. Zhou, X. Kong, M. Strømme and C. Xu, Efficient Solar Thermal Energy Conversion and Utilization by a Film of Conductive Metal–Organic Framework Layered on Nanocellulose, ACS Mater. Lett. 4 (2022) 1058-1064, https://doi.org/10.1021/acsmaterialslett.2c00190.

[53] L. Hou, N. Wang, L.-J. Yu, J. Liu, S. Zhang, Z. Cui, S. Li, H. Li, X. Liu, L. Jiang and Y. Zhao, High-Performance Janus Solar Evaporator for Water Purification with Broad Spectrum Absorption and Ultralow Heat Loss, ACS Energy Lett. 8 (2022) 553-564, https://doi.org/10.1021/acsenergylett.2c02567.

[54] Y. Shang, B. Li, C. Xu, R. Zhang and Y. Wang, Biomimetic Janus photothermal membrane for efficient interfacial solar evaporation and simultaneous water decontamination, Sep. Purif. Technol. 298 (2022) 121597, https://doi.org/10.1016/j.seppur.2022.121597.

[55] S. L. Wu, L. N. Quan, Y. T. Huang, Y. T. Li, H. C. Yang and S. B. Darling, Suspended Membrane Evaporators Integrating Environmental and Solar Evaporation for Oily Wastewater Purification, ACS Appl. Mater. Interfaces 13 (2021) 39513-39522, https://doi.org/10.1021/acsami.1c12120.

[56] H. Cao, S. Zhang, T. Jiang, D. Wang, Y. Zhu and Z. Bian, Preparing photo-thermal conversion membrane with CuS-Multi walled carbon nanotube (MWCNT) composite for solar-driven interfacial evaporation, Mater. Lett. 317 (2022) 132145, https://doi.org/10.1016/j.matlet.2022.132145.

[57] S. Wang, Y. Niu, L. Yan, W. Chan, Z. Zhu, H. Sun, J. Li, W. Liang and A. Li, Polyimide-based superhydrophilic porous membrane with enhanced thermal insulation for efficient interfacial solar evaporation, Compos Sci Technol 228 (2022) 109683, https://doi.org/10.1016/j.compscitech.2022.109683.

[58] J. Gu, P. Xiao, J. Guan, F. Ni, C. Zhang, W. Yang, Q. Liu and T. Chen, Coral-like hierarchically nanostructured membrane with high free volume for salt-free solar-enabled water purification, Mat. Today Phys. 25 (2022) 100715, https://doi.org/10.1016/j.mtphys.2022.100715.

[59] C. Cai, Y. Wang, Z. Wei and Y. Fu, Biomimetic 3D Membranes with MXene Heterostructures for Superior Solar Steam Generation, Water Treatment, and Electricity Generation, Sol. RRL 5 (2021) 2100593, https://doi.org/10.1002/solr.

202100593.

[60] H. Liu, J. Gu, Y. Liu, L. Yang, L. Wang, J. Yu and X. Qin, Reconfiguration and self-healing integrated Janus electrospinning nanofiber membranes for durable seawater desalination, Nano Res. 16 (2022) 489-495, https://doi.org/10.1007/s12274-022-4733-4.

[61] L. Ying, H. Zhu, H. Huang, X. Qu, C. Wang, X. Wang, F. Duan, S. Lu and M. Du, Scalable NiCoxSy-PANI@GF Membranes with Broadband Light Absorption and High Salt-Resistance for Efficient Solar-Driven Interfacial Evaporation, ACS Appl. Energy Mater. 4 (2021) 3563-3572, https://doi.org/10.1021/acsaem.1c00008.